analytical chemistry

pubs.acs.org/ac Article

Low-Cost, User-Friendly, All-Integrated Smartphone-Based Microplate Reader for Optical-Based Biological and Chemical Analyses

José Francisco Bergua,[⊥] Ruslán Álvarez-Diduk,[⊥] Andrea Idili, Claudio Parolo, Marc Maymó, Liming Hu, and Arben Merkoçi*

Cite This: *Anal. Chem.* 2022, 94, 1271−1285 Read Online

ACCESS | Metrics & More | Article Recommendations | Supporting Information

ABSTRACT: The quantitative detection of different molecular targets is of utmost importance for a variety of human activities, ranging from healthcare to environmental studies. Bioanalytical methods have been developed to solve this and to achieve the quantification of multiple targets from small volume samples. Generally, they can be divided into two different classes: point of care (PoC) and laboratory-based approaches. The former is rapid, low-cost, and user-friendly; however, the majority of the tests are semiquantitative, lacking in specificity and sensitivity. On the contrary, laboratory-based approaches provide high sensitivity and specificity, but the bulkiness of experimental instruments and complicated protocols hamper their use in resource-limited settings. In response, here we propose a smartphone-based device able to support laboratory-based optical techniques directly at the point of care. Specifically, we designed and fabricated a portable microplate reader that supports colorimetric, fluorescence, luminescence, and turbidity analyses. To demonstrate the potential of the device, we characterized its analytical performance by detecting a variety of relevant molecular targets (ranging from antibodies, toxins, drugs, and classic fluorophore dyes) and we showed how the estimated results are comparable to those obtained from a commercial microplate reader. Thanks to its low cost (<$300), portability (27 cm [length] × 18 cm [width] × 7 cm [height]), commercially available components, and open-source-based system, we believe it represents a valid approach to bring high-precision laboratory-based analysis at the point of care.

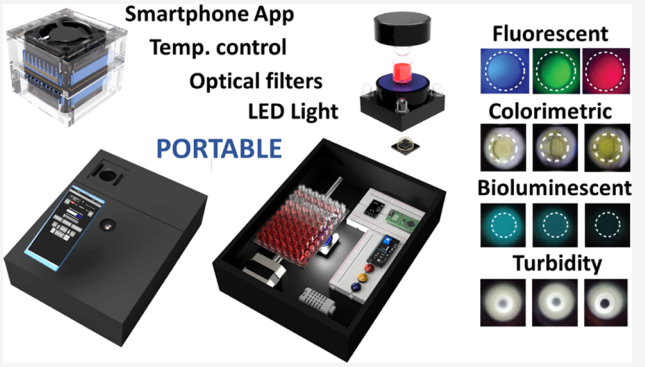

INTRODUCTION

The recent COVID-19 pandemic shows how, in our globalized world, health and environmental issues can quickly spread across the globe in a matter of days or weeks.[1,2] The realization of this new *status quo* is dramatically changing our perspective on how we are diagnosing diseases, shifting the focus from a country-focused surveillance system to a globalized one.[3−5] This new horizon forces the research community to develop more accessible and cost-effective sensing technologies. The goal is to supply every country with the best available clinical resources and know-how to diagnose and contain diseases.[6−8] To succeed in this task, the currently available and established sensing technologies allow us to pursue two different approaches. The first one is based on the use of classical point of care (PoC) sensors (i.e., lateral flow assays and electrochemical sensors such as a glucometer).[9−11] The second approach is based on the re-engineering of laboratory-based methodologies for their use at the point of care.[12−14] Undoubtedly, the former approach includes invaluable tools to carry out extensive, low-cost, and rapid testing directly in the field;[9] however, their sensitivity and limits of detection are often inappropriate to detect low concentrations of targets.[15−17] On the contrary, laboratory-based methodologies produce more precise data that allow better clinical accuracy. However, they require expensive instruments, multistep processes, and trained personnel, which strongly hamper their use in the field.[18] Despite the better analytical performance displayed by laboratory-testing methodologies, little effort has been devoted to translating them into portable, cheap, and easy-to-use analytical devices.[19] This is mainly due to the technical hurdles related to the integration of all of the hardware and software into a small device, keeping costs low.[20,21] Therefore, the development of a low-cost, portable, and easy-to-use device that is able to support laboratory-testing

Received: October 16, 2021
Accepted: December 9, 2021
Published: January 3, 2022

https://doi.org/10.1021/acs.analchem.1c04491
Anal. Chem. 2022, 94, 1271−1285

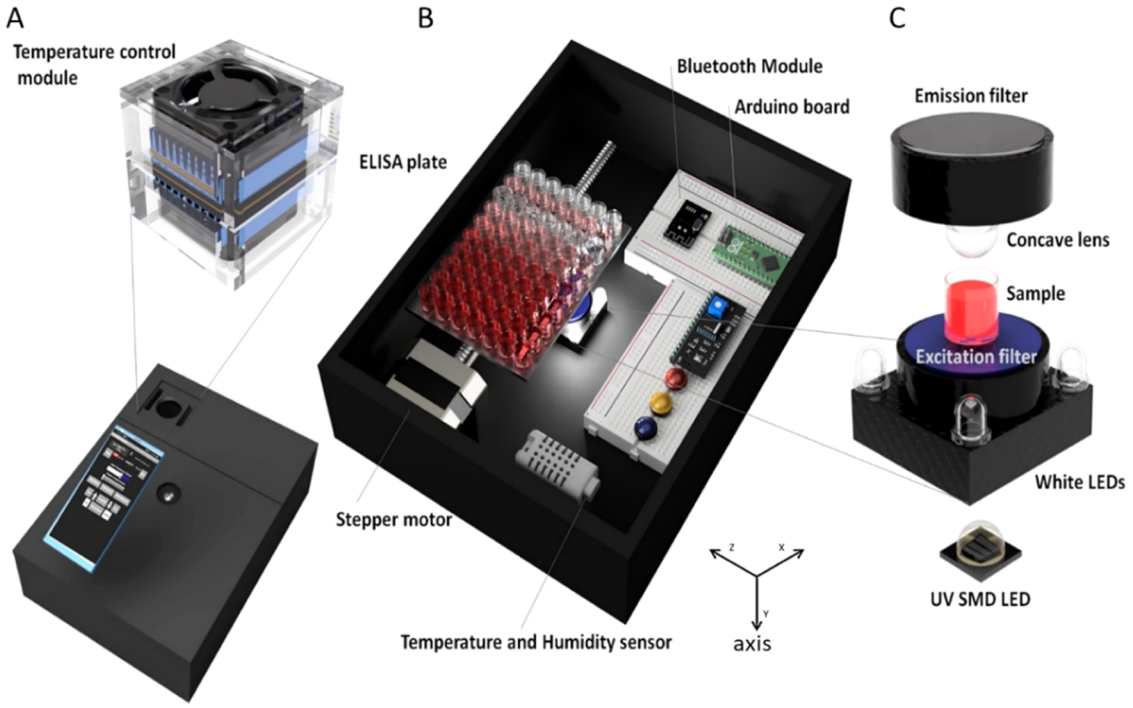

Figure 1. Schematic illustration describing the portable device. (A) When the portable platform is closed, the smartphone can be placed on top of the lid for image acquisition (bottom). At the same time, the temperature control module is placed on the top, specifically in the gap found on the top-left corner of the portable platform (top). (B) When the portable platform is open, it is possible to see the different components integrated into the case, such as the microplate (moved by the stepper motor through the *y*-axis), Bluetooth module, Arduino board, the stepper motor, the temperature, and humidity sensors. (C) Optical system of the portable platform consists of one UV SMD LED and four white LEDs, an excitation filter, an emission filter, and a concave lens to optimize the focal distance between the samples and the smartphone.

methodologies at the point of care could strongly impact our method of diagnosing and treating diseases.

Microplates are one of the most used instruments to perform laboratory-testing analysis (i.e., biochemical and cell-based assays) for clinical and biological applications.[22−24] Their success comes from their ability to process multiple samples (i.e., commonly 96 individual wells, but some can have up to 3456 wells[25]) and to support different readout strategies (i.e., colorimetric, fluorescence, and luminescence).[25] For example, microplates are commonly used as support in an enzyme-linked immunosorbent assay (ELISA), which is the gold standard test for the detection of clinically relevant antigens and antibodies.[24,26] They are also routinely used in molecular tests [i.e., polymerase chain reaction (PCR)], cell counting, and chemical and biological tests (i.e., drug-screening tests with cells, biochemical tests with bacteria, chemical characterization of fluorophores, etc.).[27−29] Contrary to the practicality of the multiwell microplate itself, microplate readers are generally bulky (i.e., not portable), delicate, and expensive (i.e., ranging between tens to hundreds of thousands of dollars) equipment.[18] These features render most of them nondeployable at the point of care, limiting their adoption in resource-limited environments, such as in low-income countries and teaching laboratories.[22] The reason behind their bulkiness and high cost is that they are meant to provide high-quality multiplex measurements in a fully automated laboratory using expensive and delicate components such as lasers, filters, and computers.[30] Fortunately, nowadays, we can find analogue components that are cheaper and can provide performance similar to their expensive counterparts.

Smartphones, cheap fabrication methods (i.e., three-dimensional, 3D printing), light-emitting diodes (LEDs), and software based on open-source systems (i.e., Arduino[31,32]) are valuable tools to achieve the democratization of the healthcare system.[18] For example, smartphones are low-cost and portable devices capable of capturing high-resolution photos, displaying enough computing power to analyze complex data through a user-friendly interface. 3D printing technologies allow the low-cost fabrication of almost any kind of object within minutes or hours using a wide range of materials (i.e., plastics, metals).[33−36] LEDs represent cheap, low-consumption, and tunable light sources that can be easily miniaturized and integrated into a portable device. Finally, open-source systems allow the control and automation of complex mechanical movements and calculus procedures without the need for expensive and delicate components. In this work, we synergically combined these tools to fabricate a low-cost (<$300), portable, plate reader capable of carrying out colorimetric, fluorescence, bioluminescence, and turbidity measurements through a commercial smartphone (Figure 1). We demonstrate how our portable reader can achieve analytical performance comparable to the classic commercial microplate readers and perform all of the experimental steps required by bioanalytical assays without the need for further instrumentations.

MATERIALS AND METHODS

Optimization of the Optical System. The resolution and clarity of the pictures captured with the portable platform are keystones of our device. Therefore, we used a convergent lens to improve the focus capability of the smartphone camera since the distance between the smartphone and the ELISA plate is very short (2.0 cm or 20 mm), which limits the focus capability

https://doi.org/10.1021/acs.analchem.1c04491
Anal. Chem. 2022, 94, 1271−1285

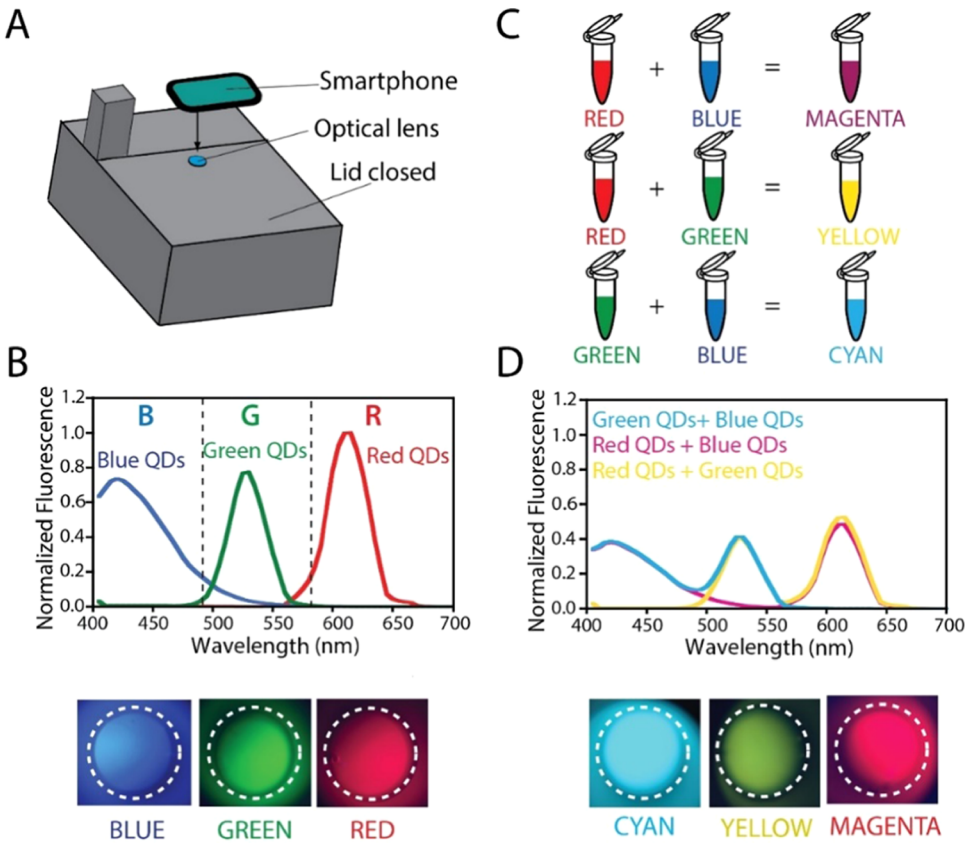

Figure 2. Fluorescence spectra measurements. (A) Microplate is located in the device and the lid is closed, and the fluorescent signal can be easily acquired through a smartphone. The image can be converted to an RGB scale, which allows the quantitative estimation of the fluorescence signal. (B) Emission spectra of the different QDs recorded with the commercial reader (top) and the corresponding pictures taken with the smartphone (bottom). (C) Combinations of different QDs yield different emission colors. (D) Emission spectra of the new combination of different color QDs read with the commercial reader (top) and the corresponding pictures taken using our portable platform (bottom).

(the shortest distance the smartphone camera can focus) of the smartphone cameras and the proper resolution of the images. In this regard, we optimized the focal length required by the optical lens using the following formula

$$\frac{1}{f} = \frac{1}{d} + \frac{1}{d'} \quad (1)$$

where "f" is the desired focal length, "d" is the real distance between the smartphone camera and the surface of the liquid sample to be analyzed, and "d'" is the real focal length of the smartphone. We consider using 100 μL of sample per well in the ELISA plate, indicating that the real distance between the smartphone camera and the sample is 17 mm. Therefore, the required focal length of the convergent lens is around 11 mm, providing an optimal focus and the best resolution of the images captured by the smartphone.

Chemical Reagents and Materials. Provided in the Supporting Information.

Fluorescence Tests. We used the portable reader to measure the signal produced by three different fluorescent dyes. More specifically, we used Q21341MP red quantum dots (QDs) (excitation 365 nm, emission 615 nm), blue QDs (excitation 365 nm, emission 420 nm), and Q21321MP green QDs (excitation 365 nm, emission 530 nm). We demonstrate that our device can detect different emission wavelengths (QDs can all be excited at 365 nm independently of the emission spectra). Specifically, we measured both individual QDs (producing red, green, and blue emissions) as well as their combinations (to produce cyan, yellow, and pink emission spectra). To perform the measurement, we used Nunc 96-well black plates with transparent bottom wells because the black plates hinder the cross-contamination of light between wells while the transparent bottom wells allow the samples to be excited from the light source. Then, we selected the optimal concentration for each dye using a commercial reader. Specifically, we tested different concentrations of QDs diluted in Milli-Q water and we selected those that provided a similar emission intensity for the three dyes (i.e., 25 nM for red QDs, 200 nM for green QDs, and 50 nM for blue QDs) (Figure 2B). After that, we used 50 μL of each solution containing the QDs as the working volume and recorded their fluorescence signal through our portable platform. Next, to obtain different emission colors, we mixed and combined 25 μL of each of the red (25 nM), green (200 nM), and blue (50 nM) QDs (Figure 2C,D). Specifically, the mixing and combination of red QDs and blue QDs yielded magenta color, the combination of red QDs and green QDs yielded yellow color, and the combination of blue QDs and green QDs yielded cyan color.

To estimate the limit of detection (LoD) of the portable and the commercial microplate reader for a dye, we measured the minimum concentration of the selected fluorescent label able to generate an instrumental signal of three times the standard deviation of the background signal. Specifically, the limit of detection was estimated using the following equation in SigmaPlot (v 14.5)

https://doi.org/10.1021/acs.analchem.1c04491
Anal. Chem. 2022, 94, 1271−1285

$$\mathrm{LOD} = [\mathrm{Dye}] \cdot \frac{3 \cdot \sigma_{\mathrm{BLANK}}}{(F_{\mathrm{DYE}} - F_{\mathrm{BLANK}})} \quad (2)$$

where [Dye] is the concentration of the dye, σ_{BLANK} is the standard deviation of the fluorescent signal in the absence of the dye, F_{DYE} is the fluorescence signal emitted by the dye, and F_{BLANK} is the fluorescence background signal.

Colorimetric ELISA Tests. To perform ELISA assay, we used 96-well white clear bottom microplates (Fisher Scientific) to avoid the well-to-well cross-contamination of light of fully transparent plates. We followed a standard immune-sandwich ELISA protocol for the detection of the SARS-CoV-2 nucleoprotein antigen, which was recently developed by our group (Figure 4). First, we coated the wells using 100 μL of a solution of a capture antibody (polyclonal, 40588-T62, SinoBiological) at a concentration of 5 μg/mL prepared in 0.05 M carbonate-bicarbonate buffer (CBS), pH 9.6, for 16 h at 4 °C. Next, we performed a washing step using 100 μL of washing buffer per well (0.01 M phosphate buffer saline at pH 7.4, 0.05% Tween-20), and then we added 3% bovine serum albumin (BSA) (in phosphate-buffered saline, PBS buffer) as a blocking agent for 2 h at 37 °C. Of note, the blocking agent allows coating the uncovered area (without the primary antibodies) on the ELISA wells to prevent further unspecific adsorption of other biomolecules present in the sample during the immunoassay. We then performed another washing step using the washing buffer. After this step, we added different concentrations of nucleoprotein (from 1 ng/mL to 1 μg/mL) dissolved in PBS (0.01 M, pH 7.4) to the wells. We let the solution incubate for 1 h at 25 °C, washed the wells three times (using the washing buffer), added the detection antibodies (monoclonal, MA1-7403, ThermoFischer) and let them incubate for 1 h at 25 °C. After this step, we washed the plate three times with the washing buffer and added the anti-mouse IgG (modified with horseradish peroxidase, HRP) for 1 h at 25 °C at a concentration of 0.05 μg/mL prepared in PBS (0.01 M, pH 7.4). Finally, after washing the plate three times with the washing buffer, we proceeded with the addition of 100 μL of the colorimetric substrate (tetramethylbenzidine, TMB) at a concentration of 0.1 M; then, after 20 min, we added 50 μL of 1 M H_2SO_4 to stop the enzymatic reaction. After this last step, we collected the colorimetric signal using both a commercial reader (using dual-wavelength detection at 450 nm to quantify the biochemical oxidation of TMB and at 620 nm to lessen unspecific absorptions from the media) and our portable reader using the smartphone.

For the second ELISA test, we followed a standard immune-sandwich ELISA protocol for the detection of human immunoglobulin G (human IgG) (Figure S11). First, we added 100 μL of anti-HIgG antibody at 2 μg/mL diluted in carbonate-bicarbonate buffer (CBS; 0.05 M, pH 9.6) to coat the ELISA wells overnight at 4 °C. Then, we removed the solution and washed the wells three times using 250 μL of the washing buffer (0.01 M phosphate buffer saline at pH 7.4, 0.1% Tween-20), followed by the addition of 200 μL of 3% BSA (w/v) (in PBS buffer) as the blocking agent for 1 h at 37 °C and repeated the washing step afterward. Next, we added 100 μL of human IgG diluted in PBS (0.01 M, pH 7.4) at different concentrations to the wells precoated with anti-HIgG antibody and incubated for 45 min at 37 °C. After this step, we removed the solutions and added 100 μL of a solution containing the anti-HIgG antibody at 0.05 μg/mL in PBS to the wells and incubated for 30 min at 37 °C. Then, we added 100 μL of HRP−streptavidin (0.05 μg/mL) to the wells and incubated for another 30 min at 37 °C. Of note, it is crucial to perform three to five repetitions of washing steps after every incubation process to avoid the unspecific binding of biomolecules, which could lead to false-positive signals. Finally, we added 100 μL of TMB (substrate solution) to the wells and incubated for 20 min at 37 °C, followed by the addition of 50 μL of 1 M H_2SO_4 (stop solution). The plates were immediately read either with the commercial reader (using dual-wavelength detection at 450 nm to quantify the biochemical oxidation of TMB and at 620 nm to lessen unspecific absorptions from the media) or with the portable reader.

Data Analysis of the Colorimetric ELISA Tests. Although the commercial reader can selectively and specifically read the yellow optical signal from the wells using the absorbance value at 450 nm, the smartphone camera only captures the image but cannot directly quantify the color intensity. To overcome this, we used ImageJ to analyze the pictures collected after the ELISA tests. Specifically, we converted the yellow color to a pale gradient into a white to black gradient, which can be easily analyzed by ImageJ. To achieve this, we exported the pictures obtained within the portable platform using the smartphone camera to the software ImageJ. Then, we set the hue threshold (range of hue values in the HSL encodings of the RGB system) between 35 and 45, corresponding to the yellow color in ImageJ, which turns the yellow color to black. Once the black to white images were obtained, we quantified the color intensity of the area corresponding to the microplate wells as follows: the whiter the images, the higher the values, whereas the darker the images, the lower the values. Afterward, we plotted these data on a scatter diagram and compared the results obtained by the commercial reader and the portable platform using the concentration of antigen (i.e., nucleoprotein or human IgG) as the *x*-axis and the colorimetric signals recorded as the *y*-axis. The resultant data were fitted using a four-logistic equation in SigmaPlot (v 14.5)

$$S_{[\mathrm{Target}]} = S^{\mathrm{MAX}}_{[\mathrm{Target}]} + \frac{(S^{0}_{[\mathrm{Target}]} - S^{\mathrm{MAX}}_{[\mathrm{Target}]})}{\left[1 + \left(\frac{[\mathrm{Target}]}{C_{50\%}}\right)^{b}\right]} \quad (3)$$

where $S_{[\mathrm{Target}]}$ is the colorimetric signal in the presence of different concentrations of the target, [Target] is the target concentration, $S^{\mathrm{MAX}}_{[\mathrm{Target}]}$ is the colorimetric signal seen at saturating concentrations of the target, $S^{0}_{[\mathrm{Target}]}$ is the background signal seen in the absence of the target, $C_{50\%}$ is the midrange concentration of target (inflection point), and b is the slope factor.

Bioluminescent Assays. To grow *Aliivibrio fischeri* for the toxicity measurements, we thawed at room temperature a stock culture of *A. fischeri* frozen at −80 °C for 10 min. Then, we added 2.5 μL of this stock culture to 25 mL of marine broth (MB medium), and the culture was left to grow at 25 °C and 135 rpm (orbital shaking) for 20 h (SSM1 mini orbital shaker from Stuart). Our MB medium contains 0.5% tryptone (w/v), 2% NaCl (w/v), 0.3% yeast extract (w/v), and 0.3% glycerol (v/v) dissolved in Milli-Q water.[37] We monitored the bacterial growth by measuring the bioluminescence produced in the commercial reader resulting always in an optimal growth between 20 and 24 h after inoculation in the raw media. Once the cellular density reached at least 10^8 CFU/mL and bioluminescence was higher than 10^6 dimensionless units

https://doi.org/10.1021/acs.analchem.1c04491
Anal. Chem. 2022, 94, 1271−1285

(recorded with the commercial reader SpectraMax iD3), we used our plate reader to carry out the bioluminescent assay (please refer to Figure S18 in the Supporting Information, SI for a detailed explanation of the bacterial growth protocol). We mixed 50 μL of bacteria and 50 μL of the sample [pentachlorophenol (PCP) at different concentrations diluted in 2% NaCl water] in a well and incubated them under agitation using the stepper motor (using the agitator functionality of the reader) for 5 min. Eventually, individual pictures from each well were captured with the smartphone using ISO 1000 and different integration times. The pictures captured with the smartphone were later analyzed using the software ImageJ (version 1.53h).

To quantify the toxicity of PCP over *A. fischeri*, we determined the EC_{50} (half-maximal effective concentration) for both the portable and the commercial microplate readers. We measured the bioluminescence intensity of the bacteria after the exposure to different concentrations of PCP for 5 min and subtracted the value of the blank (growth media without bacteria) from all of the measurements. Afterward, we divided all of the values by the bioluminescence of the control culture (bacteria without antibiotic) and plotted all of the results on a scatter diagram to calculate the EC_{50} values for each reader, with the *x*-axis being the concentration of PCP and the *y*-axis the normalized bioluminescence. Specifically, the EC_{50} was estimated using the following equation in GraphPad Prism (v 8.0.1.244)

$$y = \text{bottom} + \frac{(\text{top} - \text{bottom})}{(1 + 10^{(x - \log EC_{50})})} \tag{4}$$

where x is the concentration of PCP, y is the bioluminescence output of the bacteria, Top and Bottom are parameters calculated by the software after the mathematical adjustment and fitting of all of the data, and EC_{50} is the concentration of PCP that inhibits 50% of the bacterial bioluminescence.

Description of the Production of Wax-Patterned Circles. We created a matrix (12 × 8) of circles of 0.108 cm in diameter aligned at a distance of 0.905 cm from each other (distance between each well of the 96 ELISA plate) so that every circle is in the center of each well. The design was printed on a poly(ethylene terephthalate) (PET) substrate of 12.5 × 8.2 cm using a wax (solid-state) printer (Xerox ColorQube 8570DN) in black color. It should be noted that other types of printers (consumer inkjet or laser printer) can be used; however, wax printing has a transmittance of 0% and produces a pure black color. In this way, maximum efficiency in terms of contrast is achieved.

Bacterial Culture and Drug Screening. We grew *A. fischeri* in marine broth (MB) at 25 °C either in an orbital agitator or within the portable platform under shaking conditions (20 h cultivation). We grew the two strains of *Escherichia coli* and *Salmonella typhimurium* in tryptic soy broth (TSB) at 37 °C either in the incubator or within the portable platform (18 h cultivation) without any shaking (Figure S20). The growth was monitored by including blank samples (media without bacteria) and comparing the optical density at 600 nm of the cultures with and without bacteria after the incubation process.

We diluted the bacterial cultures to normalize the bacterial concentration to $2{\cdot}10^8$ CFU/mL (corresponding to a value of optical density of 0.2 au) by adding the appropriate volume of growth media to reach a final volume of 50 μL. Next, we added 50 μL of antibiotics at different concentrations (from 0 to 125 μg/mL diluted in appropriate growth media) to the ELISA wells containing 50 μL of bacteria. This step was followed by an incubation step performed at 25 °C with shaking for *A. fischeri* and at 37 °C without shaking for *E. coli*. Eventually, we determined the bacterial growth using the commercial reader to measure the OD_{600} and the smartphone together with the portable platform to analyze the turbidity of the media based on the dark wax-patterned circles. Briefly, to increase the contrast between the growth media and the media containing a high concentration of bacteria, a dark spot of wax printed over a white paper was placed at the center below the ELISA wells. This new method allows for increasing the contrast between those samples containing low concentrations of bacteria (darker spot, light not reflected) and high concentrations of bacteria (whiter spot, light reflected by the presence of particles [bacterial cells] within the media), boosting the sensitivity of the detection of bacterial growth within the portable platform.

We determined the % of bacterial growth for both the portable and the commercial microplate readers to quantify the antimicrobial capacity of the antibiotics against the different strains of bacteria. We measured the turbidity of the media according to the method previously explained, where the absence of bacterial growth due to a high concentration of antibiotics yields a darker wax circle than the growth of bacteria that yields a wither wax circle. First, we subtracted the value of the blank (growth media without bacteria) from all of the measurements. Afterward, we divided all of the values by the turbidity value obtained with the control culture (bacteria without antibiotic) and plotted all of the results on a scatter diagram to calculate the corresponding EC_{50} values, with the *x*-axis being the concentration of antibiotic in μg/mL and the *y*-axis the growth percentage (growth %, au) corresponding to the normalized turbidity of the media. Specifically, the % of inhibition was estimated using the following equation in SigmaPlot (v 14.5)

The equation for drug screening using the commercial reader

$$\%\ \text{growth inhibition} = \frac{(OD600_{\text{sample}} - OD600_{\text{blank}})}{OD600_{\text{noantibiotic}}} \times 100 \tag{5}$$

The equation for drug screening using the portable platform

$$\%\ \text{growth inhibition} = \frac{(I_{\text{sample}} - I_{\text{blank}})}{I_{\text{noantibiotic}}} \times 100 \tag{6}$$

$OD600_{\text{sample}}$ refers to the optical density at 600 nm of the bacterial growth with a certain concentration of antibiotic, whereas $OD600_{\text{blank}}$ refers to the optical density of the raw media without bacteria and $OD600_{\text{noantibiotic}}$ refers to the optical density of the bacterial growth without any antibiotic in the equation used for the commercial reader. In this sense, the subscripts used for intensity (i.e., I_{sample}) in the equation used for the portable platform refer to the same parameters.

RESULTS AND DISCUSSION

Optical and Mechanical Platform Design. Our portable reader is a rectangular-shaped box (27 cm [length] × 18 cm [width] × 7 cm [height]) made of polyoxymethylene, which is designed to contain all of the hardware components (i.e.,

https://doi.org/10.1021/acs.analchem.1c04491
Anal. Chem. 2022, 94, 1271−1285

electronic, mechanical, and optical) required to perform the different bioanalytical tests (Figure 1). As an optical reader, we used a commercial smartphone, which also allows controlling the different components of the device through an integrated app (Figures 1A and S3A). To make the overall device more versatile and easier to use, we incorporated a sliding lid into the device to allow easy loading of the plate and correct acquisition of the image by the smartphone. Specifically, the optical lens on the lid indicates where the smartphone should be placed to keep its camera aligned to the selected well (Figure 1A, bottom). At the same time, the lid guarantees stable lighting conditions to obtain reproducible images that can be quantitatively analyzed. We installed several functional components inside the device: an Arduino microcontroller, the thermoelectric module, a linear actuator coupled with a stepper motor, the optical system, humidity, and temperature sensors, and the complementary electronic elements (i.e., motor driver, resistors, LEDs, etc.) (Figure 1B). All of these components are commercially available, and we selected them to keep the overall cost of the device below $300 (Table S1). Of note, we did not include the price of the phone (Huawei P20 Lite) in the overall cost of the device because it may vary from country to country and brand to brand and because smartphones are widespread and used all over the world. In 2021, for example, the number of smartphone users in the world stood at 6.378 billion, which is over 80% of the world population.[38]

To monitor and precisely select the temperature inside the device, we installed a thermoelectric module (also known as a Peltier module), which works in combination with the temperature and humidity sensors (Figure 1A, top). Indeed, through the smartphone app, we can precisely and quickly (minutes) set specific temperature conditions. The module includes two heat sinks and two fans that allow the automatic and rapid change of the temperature gradient without the need for user intervention (Figure S1). Specifically, we can lower the temperature up to 7 °C and increase it by more than 30 °C; therefore, if the room temperature is 25 °C, we can cover the temperature range from 18 to 57 °C (Figure S2). At the same time, to precisely control the moving and the shaking of the plate inside the device, we integrated a stepper motor in the supporting frame (Figure 1B). Specifically, this component is integrated into the mechanical frame (linear actuator) and is designed to house a 96-well plate. Thanks to its spatial fine-tuning, it is possible to correctly align all of the optical parts with every single well of the plate. To minimize the size of the unit, the movement of the plate is automatized (again using the smartphone) on the *z*-axis (from well 1 to 12), while the movement on the *x*-axis can be performed only manually by placing the desired microplate row aligned with the smartphone camera on top. Additionally, the activation of the motor can be programmed to shake (linear movement up to 160 rpm) the plate, supporting all of the conjugation and incubation steps that are critical in many bioanalytical assays (i.e., ELISA or cell cultures).

The core of the device is the optical system, which is composed of an emission filter, a microlens (to decrease the focal distance; for more details, see the Materials and Methods section), an excitation filter, and light-emitting diodes as excitation sources (Figure 1C). Specifically, the first two components are integrated into the lid of the device, and they are located between the smartphone (used to acquire the images) and the 96-well plate (i.e., containing the different samples to be analyzed). The emission filter (long-pass filter 400 nm) allows avoiding the collection of the light coming from the excitation source, thereby reducing the background signal observed in the pictures captured using the smartphone. The light source is located on the bottom (within the portable platform) and exploits five LEDs (Figure 1C): one UV LED with an excitation wavelength at 365 nm to support fluorescence assays and four white LEDs to support different colorimetric assays. To carefully select the correct excitation wavelength, we combined the UV LED with an excitation filter (bandpass 370 nm) to perform fluorescence-based assays and improve the acquisition of the optical signal.

Finally, the smartphone plays a key role because it allows us to acquire the image directly from the well plate and collect the optical signal. In this work, we used a smartphone (Huawei P20 Lite) introduced into the market (in the midrange) almost 4 years ago, which displays a camera of 16 MegaPixels, a diaphragm aperture of f/2.2, a sensor size of 1/3.1″, and a pitch size of 1.1 μm. These represent the minimum requirements that the smartphone must display to obtain the same results we obtained and described throughout this work. Moreover, taking into account that manufacturers are currently producing smartphones using better sensors and optics in the low-/midrange of the market, the use of a new and different smartphone can only positively affect the acquisition of the image from the well plate, improving the overall sensitivity of the device.

Automation, Interface Design, and Device Operation. The functional core of our device is shared by the Arduino microcontroller and the smartphone through a dedicated app, which allows them to work in synergy, making the device intuitive and easy to use. Specifically, we created the app using MIT App Inventor 2, an open-source web application that allows newcomers to computer programming to create application software.[38,39] The graphic user interface (GUI) of our app is shown in Figure S3, together with all of the blocks containing the logical instructions for programming it. The app is connected to the Arduino device through a Bluetooth connection. The GUI is designed to contain several buttons and sliding bars to select and control the operation of the portable reader (i.e., read temperature and humidity; type of assay: colorimetric, fluorescence, bioluminescence; incubation, alignment, temperature adjustment; and the number of measurements) (Figure S3A). Of note, there are commercially available apps to read 96-well microplates. However, they have three main limitations compared to our system. First, they generally perform just only one kind of measurement, while our system can perform four different measurements (fluorescence, colorimetric, luminescence, and turbidity). Second, since they are independent of hardware, their results may be affected by different lighting conditions. Finally, being commercially available, the user has limited possibilities to adapt the app to their specific needs.

For a better understanding, most of the applications (concerning their interaction with the Arduino) are designed to send a number via Bluetooth to the microcontroller that interprets it as an action to be performed (Figure S3B). For instance, to perform a colorimetric test, we need only to press the associated button of the app, which sends the number (13). On pressing the associated button, the Arduino powers up the digital pin defined as pinWhite (white light), the app opens the camera to capture a picture of the first well, and next, send the number (41) to the Arduino to move the

https://doi.org/10.1021/acs.analchem.1c04491
Anal. Chem. 2022, 94, 1271−1285

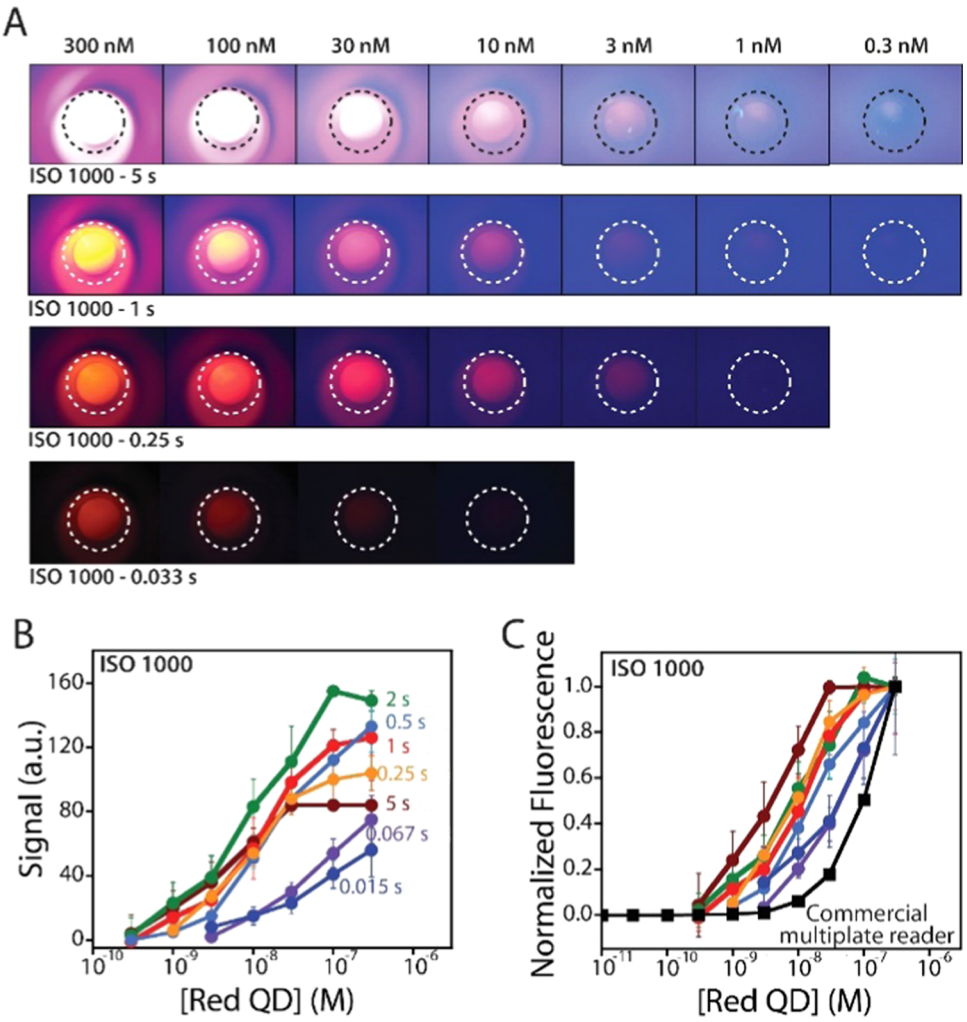

Figure 3. Fluorescence measurements. (A) Images of different concentrations of red QDs captured using different smartphone camera settings (same ISO value [1000] and varying integration time values [from 5 to 0.033 s]). (B) Calibration curves obtained to estimate the sensitivity and the limit of detection (LoD) of our platform. We used red QDs as a testbed and modulated both the LoD and sensitivity of our optical platform using different integration times with the smartphone camera (absolute values). (C) Comparison of the normalized calibration curves obtained with the commercial reader (black curve) and the portable platform. The "error bars" we report for fluorescent measurements reflect standard deviations derived using three independent replicates.

stepper motor to the next well (710 steps is the distance from well to well). In this process, there is a variable that counts the number of times that this cycle is repeated and can be modified to achieve a specific number of measurements. The rest of the assays work similarly. Fluorescence turns on the UV LED while Bioluminescence keeps the device dark. To better understand this part, see the Arduino Sketch file and the connection diagram Figure S4. Finally, a demonstration of the device in a real working environment can be seen in Movie S1.

Fluorescence Test. Our portable reader allows measuring the fluorescence signal emitted from standard dyes showing its ability to support multiplexed analysis like commercial microplate readers. Fluorescence is widely exploited as a signal readout for the detection of many clinically relevant biomarkers, thanks to its high sensitivity and rapid detection.[40,41] Despite its advantages, the application of fluorescence-based diagnostic techniques in low-resource scenarios has been hampered by the use of bulky, fragile, and expensive instruments.[33,42] To demonstrate the ability of our device to selectively detect different fluorescence signals, we used a set of three fluorophore molecules as a testbed. Specifically, two are commercially available (i.e., Q21341MP red QDs and Q21321MP green QDs from Fisher Scientific) and the third one (blue graphene QDs) was synthesized following a previous protocol.[43] We selected these dyes because they display similar absorption spectra, and so they can be excited with similar efficiency by the same optical source, a UV LED at 365 nm (Figure S5A). Next, we collected the images from wells containing different solutions of the three dyes at nanomolar concentrations (Figure 2A). We find that the optical filters used for the excitation (bandpass at 370 nm) and emission (long-pass at 400 nm) allow the smartphone reader to detect only the fluorescence signal emitted by each single dye (Figure 2B). More specifically, the conversion of the optical signal to the RGB scale allows obtaining blue, green, and red colors, which correspond to the expected fluoresce signals emitted from three dyes (Figure 2B; for image acquisition and analysis procedure, see Figure S6).

The images acquired by the smartphone demonstrate the ability of our system to detect all of the different RGB secondary colors associated with the corresponding emission spectra. To challenge our device, we tested it against solutions

https://doi.org/10.1021/acs.analchem.1c04491
Anal. Chem. 2022, 94, 1271−1285

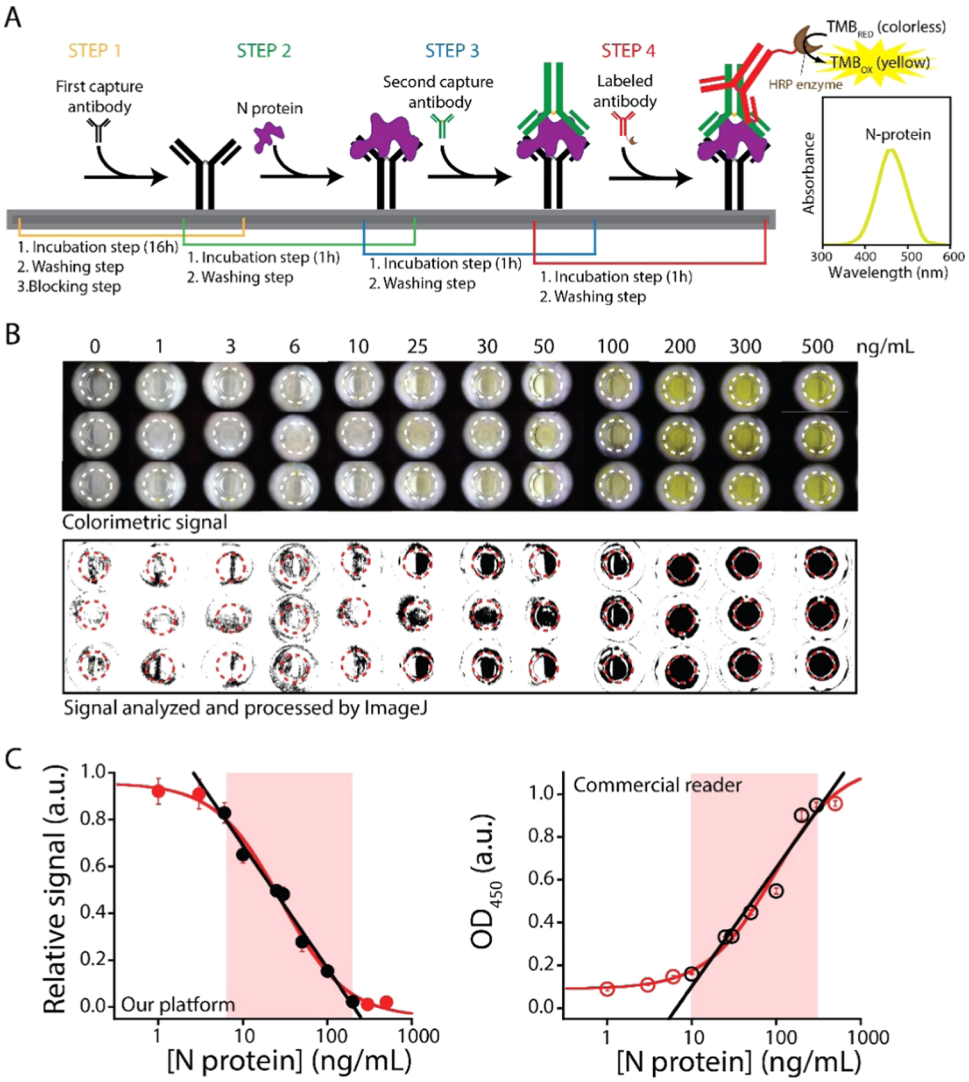

Figure 4. Colorimetric measurements. (A) Schematic of the colorimetric detection of the N-protein from SARS-CoV-2. In step 1, the first capture antibody is attached to the microwell, and then the microwells are washed and blocked with BSA (See Colorimetric ELISA Tests in Materials and Methods). In step 2, the N-protein (i.e., the target analyte) is added to the microwells, and the unbound proteins are removed using a washing buffer. In step 3, a second capture antibody is added and incubated to allow the binding with the N-protein previously captured by the first capture antibody. In step 4, after an additional washing step, an antibody labeled with the HRP enzyme can recognize the second capture antibody. After a final washing step, the enzymatic substrate TMB is added to the solution, and the intensity of the generated yellow color is correlated to the concentration of N-protein in the sample. (B) Raw colorimetric signal (top) collected from the wells using the smartphone and their conversion to black/white scale (bottom) for the estimation of the different concentrations of the N-protein. (C) Calibration curves for SARS-CoV-2 nucleoprotein were obtained with the portable reader (left) and a commercial microplate reader (right). The error bars we report for colorimetric measurements reflect standard deviations derived using three independent replicates.

that display emission spectra composed of the sum of two optical signals. Specifically, through the precise combination of two dyes, we have created emission spectra that can be converted into a secondary color of the RGB scale (i.e., magenta, yellow, and cyan) (Figure 2C). Of note, the RGB scale is a color model in which primary colors (i.e., red, green, and blue) are combined in different proportions to produce a myriad of different colors.[44] The secondary colors are obtained when two of the primary colors at the same intensity are combined. The software ImageJ (i.e., a free software employed for the analysis of the images)[45,46] allows us to measure the intensity of individual pixels or a selected area of the image, providing quantitative data based on the RGB system by giving three numbers that correspond to the intensity of the red, green, and blue colors, respectively.[45] Furthermore, we optimized the concentrations of the previously characterized blue, green, and red QDs so that they can display the same fluorescence intensity (Figure S7). Then, we mixed red QDs at 25 nM with green QDs at 200 nM to obtain a fluorescence signal corresponding to the yellow color, red QDs at 25 nM with blue QDs at 50 nM to obtain magenta, and green QDs at 200 nM with blue QDs at 50 nM to obtain cyan (Figure 2C). Through the analysis of the acquired images, we demonstrate the ability of our system to detect the different fluorescence signals which can be converted to the expected secondary color (Figure 2D). The possibility to detect an optical signal composed of the combination of two fluorophores demonstrates the ability of the platform to fully exploit the RGB scale for multiplexing detection.[47,48]

https://doi.org/10.1021/acs.analchem.1c04491
Anal. Chem. 2022, 94, 1271−1285

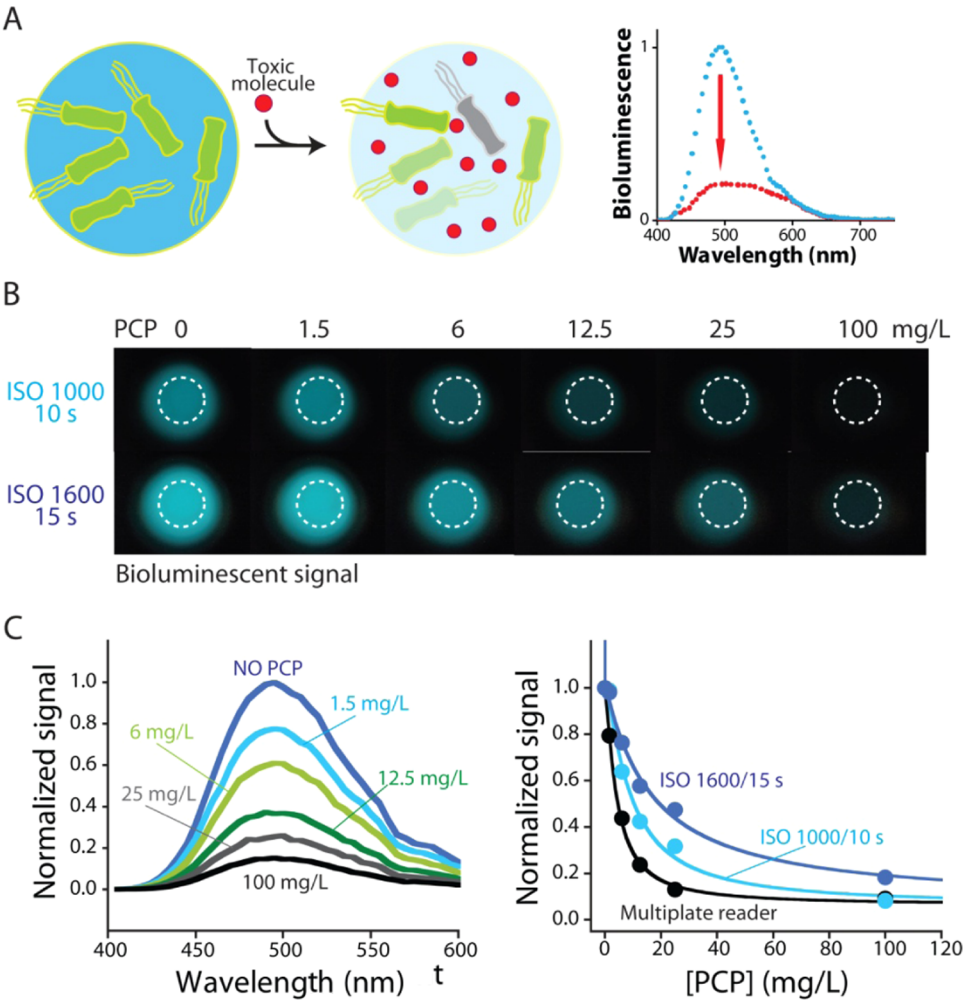

Figure 5. Bioluminescent measurements. (A) Schematic of the performance of the bioluminescent toxicity assays with *A. fischeri*. The bacteria *A. fischeri* are grown in seawater (≈2% NaCl), yielding microbial bioluminescence (on the left). Afterward, the bacteria are placed in contact with a sample containing a specific concentration of pentachlorophenol (PCP, a pesticide) after 20 h of growth (in the center). Eventually, after 5 min of incubation, the presence of a toxic substance induces a decay in the bioluminescence intensity (on the right). (B) Bioluminescence inhibition profile of *A. fischeri* obtained after 5 min of exposure to different concentrations of pentachlorophenol using a constant ISO 1600 and different integration times (10 s on top and 15 s on the bottom). (C) Presence of PCP in the samples has toxic effects on *A. fischeri* through oxidative stress and DNA mutations. Therefore, the higher the concentration of PCP, the greater harm to *A. fischeri*, and thus the stepper bioluminescence decay. On the left, bioluminescence spectra of *A. fischeri* collected at different concentrations of pentachlorophenol; on the right, normalized calibration curves describing the bioluminescence inhibition profiles of *A. fischeri* obtained with our portable platform using different smartphone camera settings (blue curves) and the commercial reader (black curve). The corresponding EC_{50} values are 8.67 mg/L for the microplate (commercial) reader, 8.76 mg/L for the conditions ISO 1000 and 10 s with the portable platform, and 8.80 mg/L for the conditions ISO 1600 and 15 s with the portable platform. The error bars we report for bioluminescent measurements reflect standard deviations derived using three independent replicates.

Finally, we demonstrate that our smartphone-based optical reader displays analytical performance comparable to commercial microplate readers. Indeed, after demonstrating the possibility to selectively detect different types of QDs and then different fluorescent signals (Figure 3), we decided to characterize our optical system through the estimation of its limit of detection (LoD) for a selected dye.[49] To do this, we used the red QDs due to their slightly higher absorbance at 365 nm, which leads to a higher fluorescence signal. Specifically, we measured the fluorescence at different concentrations of the dye, ranging from 0.1 to 300 nM. We observe that the intensity of the red color is perfectly correlated to the dye concentration (Figure 3A). Again, using ImageJ, we can easily extract the relative RGB value, which allows us to perform a quantitative measurement (for image acquisition and analysis, see Materials and Methods and Figure S6). Furthermore, to improve the detection of the fluorescence signal, we explored and characterized two parameters involved in the image acquisition: the acquisition time and the ISO of the phone camera (Figures 3A and S8). Through the rational tuning of these parameters, the device can be programmed to achieve different sensitivities (estimated by LoD from 0.1 to 3 nM) and linear ranges (between 300 and 0.1 nM; Figure 3B). To better characterize the analytical performance of the device, we compared it with a commercial reader. The estimated LoD for the commercial reader (0.14 ± 0.07 nM) is comparable to the value observed for our optical reader, such as the useful linear range (Figure 3C). Finally, to demonstrate the versatility of our device, we detected different concentrations of a second commercially available fluorophore.

https://doi.org/10.1021/acs.analchem.1c04491
Anal. Chem. 2022, 94, 1271−1285

To do this, we used fluorescein (FAM), and using the same approach, we can track its fluorescent signal estimating a LoD of 0.32 ± 0.05 μM (Figure S9). The obtained LoD, in this case, is higher than the value estimated for the commercial reader (0.14 ± 0.07 nM) because the excitation wavelength of fluorescein is around 470 nm, while the UV LED installed within the portable platform emits at 365 nm. In this sense, the LoD could be further improved by installing an excitation UV LED at 470 nm for fluorescein-related applications. This result highlights the ability of our system to perform quantitative detection of commercial fluorescent organic dyes.

Colorimetric ELISA Test. Our device can support colorimetric-based diagnostic techniques allowing the direct quantification of clinically relevant biomarkers. To evaluate its analytical performance as a testbed, we carried out the ELISA assay, which is recognized as one of the clinical gold standard techniques for the detection of protein biomarkers.[50] More specifically, ELISA tests are immunoassays used to detect analytes (i.e., antibodies, antigens, proteins, and small molecules) employing enzymatic-tagged antibodies that provide amplification of the optical output, which is directly proportional to the concentration of the analyte. Their popularity comes from their high throughput (i.e., when combined with microplates) and sensitivity (i.e., due to the enzymatic reaction) that allow measuring nanomolar and picomolar ranges of biomarkers in hundreds of patients in a single day.[51−53] Despite its clinical relevance, the long protocol (hours) based on batch processes (i.e., washing, dilutions, and incubations steps) and expensive readouts have prevented their use at the point of care or in resource-limited settings.[22] Here, the goal is not only to demonstrate the ability of our smartphone-based platform to achieve diagnostic data but also to make the overall assay more user-friendly through the use of a single device. Specifically, the versatility of our system helped us to perform all of the critical steps required for the preparation of the assay. For example, the temperature sensor and the mechanical motion (i.e., shaking of the plate) allow fully performing all of the incubation steps without the need for further instruments.

To test our smartphone-based plate reader, we challenged it with an ELISA test for the detection of the clinically relevant SARS-CoV-2 N-protein (Figure 4A). To achieve this, we developed an immune-sandwich assay based on the use of two primary antibodies, which can recognize the presence of the N-protein through the formation of a surface-adsorbed immune-sandwich complex (Figure 4A). The presence of the secondary HRP-labeled antibody (streptavidin−horseradish peroxidase) and the enzymatic substrate [i.e., tetramethylbenzidine (TMB)] allows the recognition of the sandwich complex and the quantification of the N-protein through (Figure 4B, top). Specifically, after the completion of the enzymatic reaction (15 min), the colorimetric signal is collected from each well of the plate using the smartphone. Then, the acquired images are processed and analyzed by ImageJ, and they are converted to a grayscale color to improve the contrast with the background color (Figure S10; see Materials and Methods for further details). Next, we have plotted the obtained values in function of the N-protein concentrations used during the assay, and we observe the expected sigmoidal curve (Figure 4C, left and Figure S11). Using a four-logistic equation fit, we estimated a limit of detection of 31.4 ± 0.3 ng/mL (here, the errors represent the relative standard deviation among three different wells) and a linear dynamic range that spans 2 orders of magnitude (from 30 to 1000 ng/mL). Such results are comparable to those obtained using a commercial plate reader (Figure 4C, right), where we observe a slightly lower LoD (8.74 ± 0.03 ng/mL) and a linear range spanning from 10 to 1000 ng/mL. Finally, to further demonstrate the diagnostic properties of our device, we used the same approach to detect IgG antibodies as a second biomarker observing similar analytical performance (Figure S12).

Bioluminescent Assays. The portable smartphone-based reader can also support the reading of bioluminescence, extending the possible real-world applications of the device. Over the last three decades, bioluminescent bacteria have been exploited to develop bioanalytical platforms to achieve environmental monitoring.[54−59] Their sensing mechanisms rely on the metabolic capabilities of such bacteria to produce light in response to an enzymatic reaction (carried out by a luciferase enzyme).[56,60] Because this signal is a direct indicator of their metabolic status (which is in communication with the media), its changes or variations can be used to track the presence of toxic and dangerous compounds[61−63] (Figure 5A). Here, as a testbed, we employ the bacteria *A. fischeri* (a marine Gram-negative bacteria) as a bioluminescent probe to detect the presence of the pesticide pentachlorophenol (PCP) in water.[61,64]

First, we characterized and optimized the signal acquisition process of the smartphone camera. To do this, we explored the effect of different ISO values and integration time with respect to (1) the intensity of the bioluminescence and (2) the contrast of the pictures acquired. To do this, we created a matrix of images by selecting five different ISO values (400, 640, 800, 1000, and 1600) and five different integration times (4, 6, 8, 10, and 15 s). Using these parameters, we collected the bioluminescent signal from different wells provided by bacteria (Figures 5B and S13). Comparing the different pictures, we can observe how the use of low ISO values and short integration time provides low reflection and light contamination; however, this leads to very low intensity values and contrast of the bioluminescence signal captured with the smartphone. On the contrary, high ISO values and integration time provide brighter images, but the overexposure times often lead to burned images that become tricky to analyze (Figure S12). Hence, to achieve a good compromise among bioluminescence intensity, light reflection, and optimal contrast, we selected an ISO value between 1000 and 1600 combined with a long integration time (10 and 15 s; Figure 5B).

Next, we used the portable plate reader to measure the bacteria's bioluminescence in the presence of increasing concentrations of PCP, a broad-spectrum pesticide generally found in water samples.[65,66] More specifically, PCP is metabolized into electrophilic compounds that bind to DNA and proteins, causing double and single DNA strand breaks, base oxidation, formation of reactive oxygen species (ROS), and protein adducts.[67] We tested the bacterial population against six different, environmentally relevant concentrations of PCP spanning the concentrations range from 1.5 to 100 mg/L[61,64,68] (Figure S14). As expected, the toxicity of PCP inhibits the cellular fitness of the bacteria affecting the luciferase activity, inducing a decrease in the overall bioluminescent signal (Figure 5B).[64] This behavior is further confirmed by the bioluminescence spectra, which do not display a change in the emission wavelength distribution but only in the intensity (Figure 5C, left). Plotting the bioluminescent signal as a function of the concentration of PCP, we can build toxicity

https://doi.org/10.1021/acs.analchem.1c04491
Anal. Chem. 2022, 94, 1271−1285

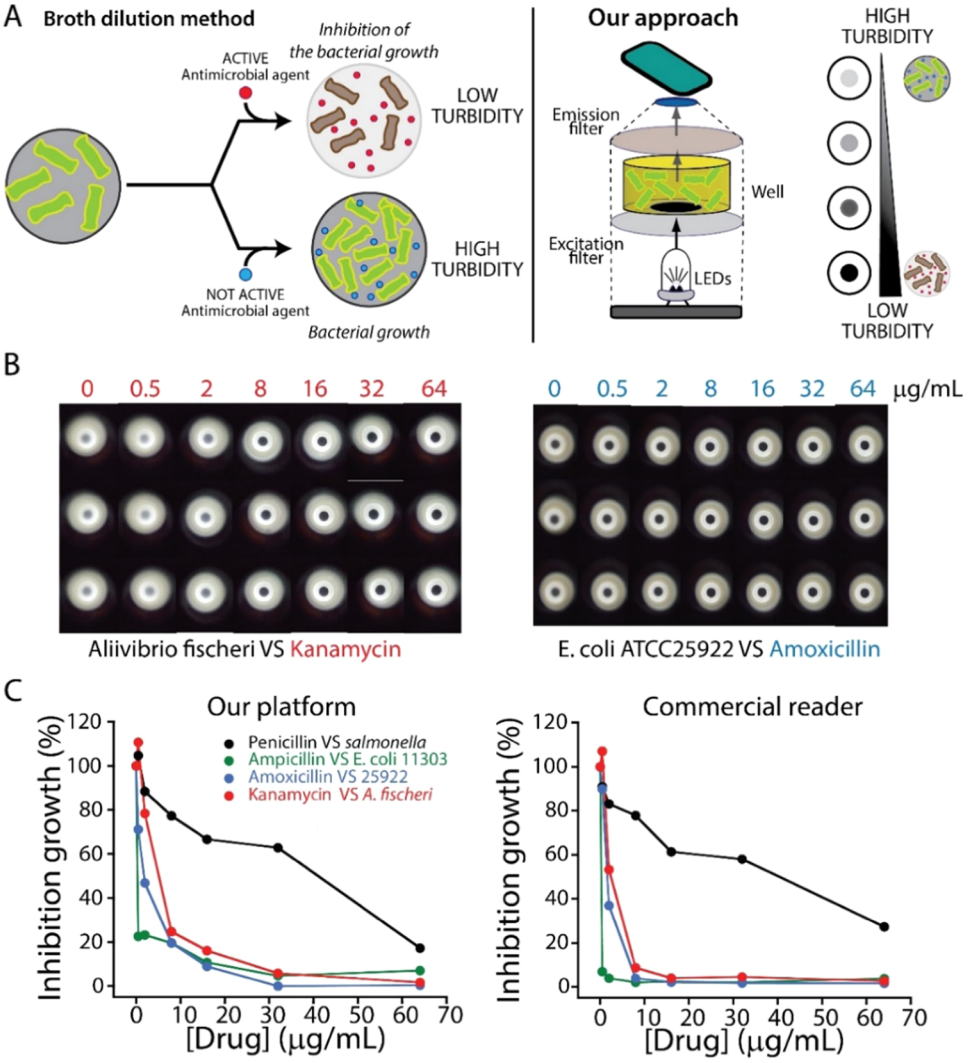

Figure 6. Turbidimetric measurements. (A) On the left: schematic of the principle underlying low bacterial concentration (=low turbidity) and high bacterial concentration (=high turbidity); the presence of an active antimicrobial agent (i.e., antibiotic) hinders bacterial growth, promoting bacterial death, and thus low turbidity media as a result of low bacterial growth. Conversely, the absence of an active antimicrobial agent does not prevent the growth of bacteria, which reach high concentrations and thus result in high turbidity media. On the right: schematic of the performance of the turbidimetric measurements using the portable platform. A dark circle made of wax is stuck on the bottom of the microplate wells, and the bacterial samples are illuminated from below with a white LED light. In the presence of many bacteria, the bacterial cells scatter the white light rays in many directions, which makes the dark wax circle appear whiter from the top, where the smartphone camera captures the images. Conversely, in the absence of bacteria, the white light rays are not scattered in such a high frequency, and thus the dark wax circle appears darker. (B) Images acquired with the smartphone and the portable platform for the growth inhibition of different bacteria using different antibiotics. On the left: samples of *A. fischeri* grown in the presence of different concentrations of kanamycin (from 0 to 64 μg/mL). The higher the concentration of kanamycin, the lower the turbidity and darker the wax circle because of the absence of bacterial growth. On the right: samples of *E. coli* ATCC25922 grown in the presence of different concentrations of amoxicillin (from 0 to 64 μg/mL). The higher the concentration of amoxicillin, the lower the turbidity and darker the wax circle because of the absence of bacterial growth. (C) Growth inhibition profiles of *E. coli* ATCC11303 corresponding to the turbidity changes under different antibiotic concentrations in the portable platform (left) and the commercial reader (right). For the commercial reader: EC_{50Pen} = 29.15 μg/mL, EC_{50Amp} = 0.04 μg/mL, EC_{50Amo} = 1.42 μg/mL, and EC_{50Kan} = 2.32 μg/mL. The error bars we report for turbidimetric measurements reflect standard deviations derived using three independent replicates.

profiles.[69,70] Then, using a sigmoidal fit, we estimated EC_{50} values[71] (i.e., PCP concentration that causes 50% bioluminescence inhibition), which correspond to 9 ± 2 and 16 ± 5 mg/L using ISO 1000/10 s and ISO 1600/15 s, respectively. These data are slightly higher than those obtained from the commercial reader (4.0 ± 0.3 mg/L) (Figure 5C, right). We believe this difference is due to two factors: the faster shaking intensity of the commercial reader that promotes aeration and thus bioluminescence and the lower sensitivity of the smartphone camera compared to the optical sensor of the commercial reader. Despite this, the device can detect the PCP in its relevant range, demonstrating again its versatility and ability to support sensing assays based on bioluminescent.[72]

Drug Screening Test. Finally, we demonstrate the use of our portable reader to perform a conventional growth inhibition assay. Generally, agar or broth dilution methods are used to determine the minimal inhibitory concentration (MIC) of antimicrobial substances[73] (Figure 6A, left). This value describes the lowest concentration of the antimicrobial agent able to inhibit the growth of a bacterial population.

https://doi.org/10.1021/acs.analchem.1c04491
Anal. Chem. 2022, 94, 1271−1285

Therefore, through its estimation, it is possible to characterize the activity of antimicrobial drugs against different bacteria, providing important information for clinicians, for example, during the selection of the pharmacological treatment.[74] Broth dilution assay is performed in test tubes, and it requires only a naked-eye reading of the visible inhibition growth.[75] During the last few decades, its miniaturization and mechanization through the use of small and disposable microdilution trays have made this method practical and very popular.[76] Using this setup, for example, the bacterial growth over time is estimated through the measurement of the turbidity, which corresponds to the absorbance value of the liquid microbial culture collected at 600 nm. So, the higher the bacterial concentration in the solution, the greater will be the scattering of light from the solution, inducing a higher absorbance value.

Having this in mind, we adapted our portable platform to support the turbidity measurements. Of note, it is extremely difficult to determine and quantify changes in turbidity with a conventional smartphone camera due to the lack of contrast between different images under the same illumination conditions.[77,78] To overcome this, we placed a dark spot below the ELISA wells to introduce a contrast between the growth media and the media containing a high concentration of bacteria (Figure S15). Specifically, we used as a template the dimensions of a 96-well plate to print a transparent PET sheet with a pattern of black wax circles (radius of 0.108 cm) centered at each well. The area of black circles is smaller than the area of the well, so this ensures the passage of light through the wells from the excitation source. Next, we placed the wax printed sheet on the bottom of the 96-well plate (stuck on the metallic plate, see Figure S15), and we tested how the presence of bacteria and its growth can affect the black color of the circular background.

Specifically, we tested solutions containing different concentrations of bacteria, and we acquired the image using the smartphone (Figure S16). To improve the analysis of the picture, we converted it to the white/black scale using ImageJ, and we sampled only the area of the black circles. We found that the black circle (not in contact with the solution) becomes whiter due to the presence of bacterial cells, which induces the scattering of the light (Figure 6A, right). Accordingly, in the presence of a higher concentration of bacteria, we observe a whiter wax circle in the smartphone images (Figure S16). Therefore, this new method allows to quantify and differentiate samples containing low concentrations of bacteria (darker spot, light not reflected) and high concentrations of bacteria (whiter spot, light reflected by the presence of particles [bacteria cells] within the media), boosting the sensitivity of the detection of bacterial growth within the portable platform (Figures 6 and S17). Finally, as demonstrated for the previous systems, to increase the sensitivity during the detection of bacterial growth, we optimized this system by exploring the smartphone camera settings (Figure S16). The best results are obtained using a single sheet of wax-patterned PET, the maximum ISO value (3200), and 1/8 s of integration time with the smartphone camera, providing a relative change of 42% between the media without bacteria (MB) and the media with bacteria ($\approx 10^9$ CFU/mL).

Next, we envisaged a direct application for these turbidity measurements. Since antibiotic resistance has become one of the major problems the healthcare system is facing nowadays,[79] the use of a portable platform to detect bacterial resistance to antibiotics provides a powerful functionality as a screening device. In this regard, we tested four different strains of bacteria (*A. fischeri*, *E. coli* ATCC11303, *E. coli* ATCC25922, and *Salmonella*) with different concentrations of four antibiotics (kanamycin, ampicillin, penicillin, and amoxicillin). After 20 h of growth (at 25 °C for *A. fischeri* and at 37 °C for *E. coli*), we evaluated the turbidity of the media [marine broth (MB) for *A. fischeri* and tryptic soy broth (TSB) for *E. coli*], estimating the optical density (OD) at 600 nm using the commercial reader (Figures S17 and S18). Through this first screening test, we selected only the couples of bacteria and antibiotics that display an inhibiting effect to repeat the measurements using our portable platform (Figure 6C). The results demonstrate the ability of our device to perform an inhibition test, and we find a correlation between the two methods, observing a slightly higher sensitivity for the commercial reader.

CONCLUSIONS

Here, we showed that by purchasing and assembling commercially available, low-cost hardware components, and using open-source software with a smartphone, it is possible to create a portable plate reader that supports optical-based analysis with analytical performance like those found in bulky, expensive commercial readers (Table S2). Specifically, we demonstrated how the portable plate reader can successfully measure fluorescent, colorimetric, bioluminescent, and turbidity signals. Subsequently, we employed it to carry out gold standard analytical assays such as an ELISA for the detection of a SARS-CoV-2 N-protein, a toxicity test measuring the effect of a pesticide on bioluminescent bacteria, and a drug-screening test checking the antimicrobial activity of four different antibiotics. Taking full advantage of the smartphone capabilities, in addition to employing it to control the device and measure the signal, we have also used it to perform multistep assays that may be easy to follow also by nonspecialized personnel. Despite the advances achieved in terms of functionality, versatility, ease of use, and portability, we believe this platform could be improved further. More specifically, sensitivity, accurate image acquisition, and data processing remain the main challenges. These can be easily improved by exploiting the modularity of the platform through the use of more expensive and better components (i.e., hardware and software), which will allow improving the performance but sacrifice the overall cost.

Although there are commercially available 96-well portable readers in the market, their cost is generally higher than 3000€ and they are designed to carry out single detection methods.[80] We believe that while they may represent a valid tool for average-funded groups that want to perform colorimetric measurements in a space-limited laboratory, they fail to provide a versatile and low-cost platform. More specifically, the portable reader we present in our manuscript is not only considerably cheaper but can also carry out fluorescence, luminescence, and turbidity measurements. Furthermore, since it is built by the user itself, it can also be easily repaired/customized using low-cost materials, whereas commercial portable readers must be sent to the factory, implying the impossibility to carry out measurements for several weeks, and, in the case the warranty is expired, it would also imply shipping and repairing costs. We hope that this work will lead the way to the adaptation of laboratory-based methods for their use at the point of care, giving healthcare workers new and effective tools to control dangerous situations and to provide the best

https://doi.org/10.1021/acs.analchem.1c04491
Anal. Chem. 2022, 94, 1271−1285

possible care independently of the resources available in each region of the world.

■ ASSOCIATED CONTENT

Supporting Information

The Supporting Information is available free of charge at https://pubs.acs.org/doi/10.1021/acs.analchem.1c04491.

Materials and methods; list of the components and their relative costs; thermoelectric module; temperature gradient; graphic user interface; electronic diagram; Arduino sketch; raw absorbance spectra and emission of three dyes; optimization of the dyes' concentrations for the RGB secondary colors; optimization of the image acquisition process; ELISA and detection of IgG antibodies; workflow for colorimetric, fluorescence, bioluminescent, and turbidity measurements; calibration curves obtained with the portable reader and the commercial reader; bacterial growth inside the device; drug screening using the spectrophotometer (PDF)

Demonstration of the portable device (Movie S1) (AVI)

■ AUTHOR INFORMATION

Corresponding Author

Arben Merkoçi − *Institut Català de Nanociència i Nanotecnologia (ICN2), 08193 Barcelona, Spain; CSIC and the Barcelona Institute of Science and Technology (BIST), 08036 Barcelona, Spain; Institucio' Catalana de Recerca i Estudis Avançats (ICREA), 08010 Barcelona, Spain;* orcid.org/0000-0003-2486-8085; Email: arben.merkoci@icn2.cat

Authors

José Francisco Bergua − *Institut Català de Nanociència i Nanotecnologia (ICN2), 08193 Barcelona, Spain;* orcid.org/0000-0002-5969-193X

Ruslán Álvarez-Diduk − *Institut Català de Nanociència i Nanotecnologia (ICN2), 08193 Barcelona, Spain;* orcid.org/0000-0002-9876-1574

Andrea Idili − *Institut Català de Nanociència i Nanotecnologia (ICN2), 08193 Barcelona, Spain;* orcid.org/0000-0002-6004-270X

Claudio Parolo − *Institut Català de Nanociència i Nanotecnologia (ICN2), 08193 Barcelona, Spain; Barcelona Institute for Global Health, 08036 Barcelona, Spain;* orcid.org/0000-0001-9481-4408

Marc Maymó − *Institut Català de Nanociència i Nanotecnologia (ICN2), 08193 Barcelona, Spain*

Liming Hu − *Institut Català de Nanociència i Nanotecnologia (ICN2), 08193 Barcelona, Spain;* orcid.org/0000-0002-8666-9287

Complete contact information is available at: https://pubs.acs.org/10.1021/acs.analchem.1c04491

Author Contributions

⊥J.F.B. and R.A.-D. contributed equally to this work. The manuscript was written through the contributions of all authors. All authors have given approval to the final version of the manuscript.

Notes

The authors declare no competing financial interest.

■ ACKNOWLEDGMENTS

ICN2 is funded by CERCA programme, Generalitat de Catalunya. Grant SEV-2017-0706 funded by MCIN/AEI/10.13039/501100011033. The authors acknowledge Consejo Superior de Investigaciones Científicas (CSIC) for the project "COVID19-122" granted in the call "Nuevas ayudas extraordinarias a proyectos de investigación en el marco de las medidas urgentes extraordinarias para hacer frente al impacto económico y social del COVID-19 (Ayudas CSIC-COVID-19)" and the research project INTCATCH 2020, Development and application of novel, integrated tools for monitoring and managing catchments supported by the European Union's Horizon 2020 research and innovation program (Grant 689341). The authors also acknowledge the project MAT2017-87202-P funded by MCIN/AEI/10.13039/501100011033/and FEDER Una manera de hacer Europa. R.A.-D. acknowledges funding from the European Union Horizon2020 Programme under Grant No. 881603 (Graphene Flagship Core 3). A.I. was supported by PROBIST postdoctoral fellowship funded by the European Research Council (Marie Skłodowska-Curie grant agreement no. 754510).

■ REFERENCES

(1) Gubrium, A.; Gubrium, E. *Lancet* **2021**, *397*, 2244−2245.
(2) Marshall, M. *Nature* **2021**, *594*, 168−170.
(3) Al-Aly, Z.; Xie, Y.; Bowe, B. *Nature* **2021**, *594*, 259−264.
(4) Maher, B.; Van Noorden, R. *Nature* **2021**, *594*, 316−319.
(5) Nsubuga, P.; White, M. E.; Thacker, S. B.; Anderson, M. A.; Blount, S. B.; Broome, C. V.; Chiller, T. M.; Espitia, V.; Rubina, I.; Sosin, D.; Stroup, D. F.; Tauxe, R. V.; Vijayaraghavan, M.; Trostle, M. *Publich Health Surveillance: A Tool for Targeting and Monitoring Interventions*; Disease Control Priorities in Developing Countries; The International Bank for Reconstruction and Development/The World Bank: Washington, 2006.
(6) Luo, Y. T.; Wang, J. H.; Zhang, M. M.; Wang, Q. Z.; Chen, R.; Wang, X. L.; Wang, H. L. *J. Clin. Lab. Anal.* **2021**, *35*, No. 1241506.
(7) Garg, A.; Ghoshal, U.; Patel, S. S.; Singh, D. V.; Arya, A. K.; Vasanth, S.; Pandey, A.; Srivastava, N. *J. Med. Virol.* **2021**, *93*, 2281−2286.
(8) Yelagandula, R.; Bykov, A.; Vogt, A.; Heinen, R.; Özkan, E.; Strobl, M. M.; Baar, J. C.; Uzunova, K.; Hajdusits, B.; Kordic, D.; Suljic, E.; Kurtovic-Kozaric, A.; Izetbegovic, S.; Schaeffer, J.; Hufnagl, P.; Zoufaly, A.; Seitz, T.; Al-Rawi, M.; Ameres, S.; Baar, J.; Bauer, B.; Beer, N.; Bergauer, K.; Binder, W.; Blaukopf, C.; Bochev, B.; Brennecke, J.; Brinnich, S.; Bundalo, A.; Busslinger, M.; Clausen, T.; de Vries, G.; Dekens, M.; Drechsel, D.; Dzupinkova, Z.; Eckmann-Mader, M.; Fellner, M.; Fellner, T.; Fin, L.; Gapp, B. V.; Grabmann, G.; Grishkovskaya, I.; Hagelkruys, A.; Handler, D.; Haselbach, D.; Hempel, L.; Hill, L.; Hoffmann, D.; Horer, S.; Isemann, H.; Kalis, R.; Kellner, M.; Kley, J.; Köcher, T.; Köhler, A.; Krauditsch, C.; Kula, S.; Lang, S.; Latham, R.; Leitner, M. C.; Leonard, T.; Lindenhofer, D.; Manzenreither, R. A.; Matl, M.; Mechtler, K.; Meinhart, A.; Mereiter, S.; Micheler, T.; Moeseneder, P.; Neumann, T.; Nimpf, S.; Nordborg, M.; Ogris, E.; Pagani, M.; Pauli, A.; Peters, J. M.; Pjevac, P.; Plaschka, C.; Rath, M.; Reumann, D.; Rieser, S.; Rocha-Hasler, M.; Rodriguez, A.; Ropek, N.; Ross, J. J.; Scheuch, H.; Schindler, K.; Schmidt, C.; Schmidt, H.; Schnabl, J.; Schüchner, S.; Schwickert, T.; Sommer, A.; Soldoroni, D.; Stadlmann, J.; Steinlein, P.; Strobl, M.; Strobl, S.; Sun, Q.; Tang, W.; Trübestein, L.; Trupke, J.; Umkehrer, C.; Urmosi-Incze, S.; Versteeg, G.; Vogt, V.; Wagner, M.; Weissenboeck, M.; Werner, B.; Zuber, J.; Födinger, M.; Allerberger, F.; Stark, A.; Cochella, L.; Elling, U. *Nat. Commun.* **2021**, *12*, No. 1243296.
(9) Mytton, O. T.; McCarthy, N.; Watson, J.; Whiting, P. *Br. Med. J.* **2021**, No. n1411.

(10) Trombetta, B. A.; Kandigian, S. E.; Kitchen, R. R.; Grauwet, K.; Webb, P. K.; Miller, G. A.; Jennings, C. G.; Jain, S.; Miller, S.; Kuo, Y.; Sweeney, T.; Gilboa, T.; Norman, M.; Simmons, D. P.; Ramirez, C. E.; Bedard, M.; Fink, C.; Ko, J.; De León Peralta, E. J.; Watts, G.; Gomez-Rivas, E.; Davis, V.; Barilla, R. M.; Wang, J.; Cunin, P.; Bates, S.; Morrison-Smith, C.; Nicholson, B.; Wong, E.; El-Mufti, L.; Kann, M.; Bolling, A.; Fortin, B.; Ventresca, H.; Zhou, W.; Pardo, S.; Kwock, M.; Hazra, A.; Cheng, L.; Ahmad, Q. R.; Toombs, J. A.; Larson, R.; Pleskow, H.; Luo, N. M.; Samaha, C.; Pandya, U. M.; De Silva, P.; Zhou, S.; Ganhadeiro, Z.; Yohannes, S.; Gay, R.; Slavik, J.; Mukerji, S. S.; Jarolim, P.; Walt, D. R.; Carlyle, B. C.; Ritterhouse, L. L.; Suliman, S. *BMC Infect. Dis.* **2021**, *21*, No. 580.
(11) Chaibun, T.; Puenpa, J.; Ngamdee, T.; Boonapatcharoen, N.; Athamanolap, P.; O'Mullane, A. P.; Vongpunsawad, S.; Poovorawan, Y.; Lee, S. Y.; Lertanantawong, B. *Nat. Commun.* **2021**, *12*, No. 1065865.
(12) Stevenson, M.; Metry, A.; Messenger, M. *Health Technol. Assess.* **2021**, *25*, 1−74.
(13) Alkharsah, K. R. *GMS Ger. Med. Sci.* **2021**, *19*, No. 1264310.
(14) Bhadra, S.; Riedel, T. E.; Lakhotia, S.; Tran, N. D.; Ellington, A. D. *mSphere* **2021**, *6*, 7−8.
(15) Bastos, M. L.; Perlman-Arrow, S.; Menzies, D.; Campbell, J. R. *Ann. Intern. Med.* **2021**, *174*, 501−510.
(16) Khorasani, A.; Chegini, A.; Mirzaei, A. *Can. Respir. J.* **2020**, *2020*, No. 962332.
(17) Silva Júnior, J. V. J.; Merchioratto, I.; de Oliveira, P. S. B.; Rocha Lopes, T. R.; Brites, P. C.; de Oliveira, E. M.; Weiblen, R.; Flores, E. F. *J. Virol. Methods* **2021**, *288*, No. 114007.
(18) Balsam, J.; Ossandon, M.; Bruck, H. A.; Lubensky, I.; Rasooly, A. *Expert Opin. Med. Diagn.* **2013**, *7*, 243−255.
(19) Stegeman, I.; Ochodo, E. A.; Guleid, F.; Holtman, G. A.; Yang, B.; Davenport, C.; Deeks, J. J.; Dinnes, J.; Dittrich, S.; Emperador, D.; Hooft, L.; Spijker, R.; Takwoingi, Y.; Van den Bruel, A.; Wang, J.; Langendam, M.; Verbakel, J. Y.; Leeflang, M. M. G. *Cochrane Database Syst. Rev.* **2020**, *2020*, 2020−2021.
(20) Hafsiya, T. H.; Rose, B. In *An IoT-Cloud Based Health Monitoring Wearable Device for Covid Patients*, 2021 7th International Conference on Advanced Computing and Communication Systems (ICACCS); IEEE, 2021; pp 266−269.
(21) Lonini, L.; Shawen, N.; Botonis, O.; Fanton, M.; Jayaraman, C.; Mummidisetty, C. K.; Shin, S. Y.; Rushin, C.; Jenz, S.; Xu, S.; Rogers, J. A.; Jayaraman, A. *IEEE J. Transl. Eng. Health Med.* **2021**, *9*, No. 4900311.
(22) Berg, B.; Cortazar, B.; Tseng, D.; Ozkan, H.; Feng, S.; Wei, Q.; Chan, R. Y. L.; Burbano, J.; Farooqui, Q.; Lewinski, M.; Di Carlo, D.; Garner, O. B.; Ozcan, A. *ACS Nano* **2015**, *9*, 7857−7866.
(23) Servais, P.; Garcia-armisen, T.; et al. *Can. J. Microbiol.* **2007**, *53*, 798−801.
(24) ThermoFisher Scientific. ELISA (Enzyme-Linked Immunosorbent Assay), 2021. https://www.thermofisher.com/es/es/home/life-science/protein-biology/protein-biology-learning-center/protein-biology-resource-library/pierce-protein-methods/overview-elisa.html.
(25) Jones, E.; Michael, S.; Sittampalam, G. *Comput. Sci.* **2016**, 1337−1363.
(26) Ciaurriz, P.; Fernández, F.; Tellechea, E.; Moran, J. F.; Asensio, A. C. *Beilstein J. Nanotechnol.* **2017**, *8*, 244−253.
(27) Allkja, J.; Bjarnsholt, T.; Coenye, T.; Cos, P.; Fallarero, A.; Harrison, J. J.; Lopes, S. P.; Oliver, A.; Pereira, M. O.; Ramage, G.; Shirtliff, M. E.; Stoodley, P.; Webb, J. S.; Zaat, S. A. J.; Goeres, D. M.; Azevedo, N. F. *Biofilm* **2020**, *2*, No. 100010.
(28) Prata, J. C.; Venâncio, C.; da Costa, J. P.; Lopes, I.; Duarte, A. C.; Rocha-Santos, T. *Mar. Pollut. Bull.* **2021**, *170*, No. 112615.
(29) Lage, O. M.; Ramos, M. C.; Calisto, R.; Almeida, E.; Vasconcelos, V.; Vicente, F. *Mar. Drugs* **2018**, *16*, No. 279.
(30) Dincer, C.; Bruch, R.; Kling, A.; Dittrich, P. S.; Urban, G. A. *Trends Biotechnol.* **2017**, *35*, 728−742.
(31) Visconti, P.; de Fazio, R.; Costantini, P.; Miccoli, S.; Cafagna, D. *J. Commun. Software Syst.* **2019**, *15*, 89−100.
(32) Kirthika, V.; Vecraraghavatr, A. K. In *Design and Development of Flexible On-Board Diagnostics and Mobile Communication for Internet of Vehicles*, 2018 International Conference on Computer, Communication, and Signal Processing (ICCCSP); IEEE, 2018.
(33) Quesada-González, D.; Merkoçi, A. *Biosens. Bioelectron.* **2017**, *92*, 549−562.
(34) Cevenini, L.; Calabretta, M. M.; Tarantino, G.; Michelini, E.; Roda, A. *Sens. Actuators, B* **2016**, *225*, 249−257.
(35) Yuk, H.; Lu, B.; Lin, S.; Qu, K.; Xu, J.; Luo, J.; Zhao, X. *Nat. Commun.* **2020**, *11*, No. 1604.
(36) Chen, Z.; Li, Z.; Li, J.; Liu, C.; Lao, C.; Fu, Y.; Liu, C.; Li, Y.; Wang, P.; He, Y. *J. Eur. Ceram. Soc.* **2019**, *39*, 661−687.
(37) *Difco & BBL Manual*, 2nd ed.; Marine Broth 2216, 2021.
(38) O'Dea, S. Number of Smartphone Users from 2016 to 2021. Statista GmbH, 2021. https://www.statista.com/statistics/330695/number-of-smartphone-users-worldwide/.
(39) APP Inventor. *MIT App Inventor 2*; Technological Institute of Massachusetts, 2021.
(40) Patton, E. W.; Tissenbaum, M.; Harunani, F. MIT App Inventor: Objectives, Design, and Development. In *Computational Thinking Education*; Springer: Singapore, 2019; pp 31−49. https://doi.org/10.1007/978-981-13-6528-7_3.
(41) Zhao, X.; Dai, X.; Zhao, S.; Cui, X.; Gong, T.; Song, Z.; Meng, H.; Zhang, X.; Yu, B. *Spectrochim. Acta, Part A* **2021**, *247*, No. 119038.
(42) Gao, L.; Wang, W.; Wang, X.; Yang, F.; Xie, L.; Shen, J.; Brimble, M. A.; Xiao, Q.; Yao, S. Q. *Chem. Soc. Rev.* **2021**, *50*, 1219−1250.
(43) Bergua, J. F.; Hu, L.; Fuentes-Chust, C.; Álvarez-Diduk, R.; Hassan, A. H. A.; Parolo, C.; Merkoçi, A. *Lab Chip* **2021**, *21*, 2417−2426.
(44) Dong, Y.; Shao, J.; Chen, C.; Li, H.; Wang, R.; Chi, Y.; Lin, X.; Chen, G. *Carbon* **2012**, *50*, 4738−4743.
(45) Naren, G.; Hsu, C.-W.; Li, S.; Morimoto, M.; Tang, S.; Hernando, J.; Guirado, G.; Irie, M.; Raymo, F. M.; Sundén, H.; Andréasson, J. *Nat. Commun.* **2019**, *10*, No. 3996.
(46) Labno, C. *Basic Intensity Quantification with ImageJ*; University of Chicago, 2021.
(47) Rasband, W. *ImageJ*; U.S. National Institutes of Health: Bethesda, Maryland, USA, 2021.
(48) Carl, P.; Sarma, D.; Gregório, B. J. R.; Hoffmann, K.; Lehmann, A.; Rurack, K.; Schneider, R. J. *Anal. Chem.* **2019**, *91*, 12988−12996.
(49) Zhang, C.; Jiang, Z.; Jin, M.; Du, P.; Chen, G.; Cui, X.; Zhang, Y.; Qin, G.; Yan, F.; Abd El-Aty, A. M.; Hacimüftüoğlu, A.; Wang, J. *Food Chem.* **2020**, *326*, No. 126813.
(50) Shrivastava, A. *Chron. Young Sci.* **2011**, *2*, 21−25.
(51) Lenquin, R. M. *Clin. Biochem.* **2005**, *51*, 2415−2418.
(52) Shirai, K.; Mawatari, K.; Ohta, R.; Shimizu, H.; Kitamori, T. *Analyst* **2018**, *143*, 943−948.
(53) Kimoto, M.; Shermane Lim, Y. W.; Hirao, I. *Nucleic Acids Res.* **2019**, *47*, 8362−8374.
(54) Guo, S.; Lakshmipriya, T.; Gopinath, S. C. B.; Anbu, P.; Feng, Y. *Nanoscale Res. Lett.* **2019**, *14*, No. 222.
(55) Sharma, P.; Asad, S.; Ali, A. *J. Biosci.* **2013**, *38*, 251−258.
(56) Menz, J.; Schneider, M.; Kümmerer, K. *Chemosphere* **2013**, *93*, 990−996.
(57) Faria, E. C.; Treves Brown, B. J.; Snook, R. D. *J. Environ. Monit.* **2004**, *6*, 97−102.
(58) Girotti, S.; Ferri, E. N.; Fumo, M. G.; Maiolini, E. *Anal. Chim. Acta* **2008**, *608*, 2−29.
(59) Roda, A. *Chemiluminescence and Bioluminescence*; Roda, A., Ed.; Royal Society of Chemistry: Cambridge, 2010. https://doi.org/10.1039/9781849732024.
(60) Visick, K. L.; Foster, J.; Doino, J.; McFall-Ngai, M.; Ruby, E. G. *J. Bacteriol.* **2000**, *182*, 4578−4586.
(61) Baldwin, T. O.; Devine, J. H.; Heckel, R. C.; Lin, J. W.; Shadel, G. S. *J. Biolumin. Chemilumin.* **1989**, *4*, 326−341.
(62) Bergua, J. F.; Álvarez-Diduk, R.; Hu, L.; Hassan, A. H. A.; Merkoçi, A. *J. Hazard. Mater.* **2021**, *406*, No. 124434.

(63) Environmental Bio-Detection Products. *Aliivibrio Fischeri Toxicity Tests*; Environmental Bio-Detection Products Inc., 2021.
(64) Jarque, S.; Masner, P.; Klánová, J.; Prokeš, R.; Bláha, L. *Front. Microbiol.* **2016**, *7*, No. 1738.
(65) Froehner, K.; Backhaus, T.; Grimme, L. H. *Chemosphere* **2000**, *40*, 821−828.
(66) Pubchem. *Pentachlorophenol*; Pubchem, 2021.
(67) Bettinetti, R.; Kopp-Schneider, A.; Vignati, D. A. L. *Sci. Total Environ.* **2018**, *613−614*, 39−45.
(68) Igbinosa, E. O.; Odjadjare, E. E.; Chigor, V. N.; Igbinosa, I. H.; Emoghene, A. O.; Ekhaise, F. O.; Igiehon, N. O.; Idemudia, O. G. *Sci. World J.* **2013**, No. 460215.
(69) Froehner, K.; Meyer, W.; Grimme, L. H. *Chemosphere* **2002**, *46*, 987−997.
(70) Mortimer, M.; Kasemets, K.; Heinlaan, M.; Kurvet, I.; Kahru, A. *Toxicol. In Vitro* **2008**, *22*, 1412−1417.
(71) Liu, J.; Morales-Narváez, E.; Orozco, J.; Vincent, T.; Zhong, G.; Merkoçi, A. *Nano Res.* **2017**, *11*, 114−125.
(72) Ventura, F. F.; Mendes, L. F.; Oliveira, A. G.; Bazito, R. C.; Bechara, E. J. H.; Freire, R. S.; Stevani, C. V. *Environ. Toxicol. Chem.* **2020**, *39*, 1558−1565.
(73) World Health Organization. *Pentachlorophenol in Drinking-Water*; World Health Organization, 2021.
(74) Wiegand, I.; Hilpert, K.; Hancock, R. E. W. *Nat. Protoc.* **2008**, *3*, 163−175.
(75) Reller, L. B.; Weinstein, M.; Jorgensen, J. H.; Ferraro, M. J. *Clin. Infect. Dis.* **2009**, *49*, 1749−1755.
(76) Balouiri, M.; Sadiki, M.; Ibnsouda, S. K. *J. Pharm. Anal.* **2016**, *6*, 71−79.
(77) Benkova, M.; Soukup, O.; Marek, J. *J. Appl. Microbiol.* **2020**, *129*, 806−822.
(78) Ceylan Koydemir, H.; Rajpal, S.; Gumustekin, E.; Karinca, D.; Liang, K.; Göröcs, Z.; Tseng, D.; Ozcan, A. *Sci. Rep.* **2019**, *9*, No. 19901.
(79) World Health Organization. *Antibiotic Resistance*; World Health Organization, 2021.
(80) Wolflabs. Microplate Readers, 2021. https://www.wolflabs.co.uk/laboratory-products/microplate-readers.

https://doi.org/10.1021/acs.analchem.1c04491
Anal. Chem. 2022, 94, 1271−1285